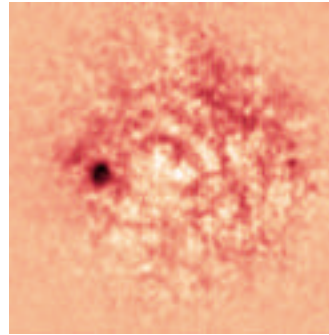
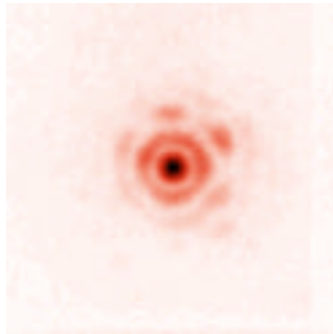


Science Concept Study Final Report

**The NGST Coronagraphic mode Study
NEF: NGST Exo-planet Finder**

Pre-phase A study report



INVESTIGATORS :

October 1, 1999

Table of contents

1.0 Science	4
1.1 Executive summary	4
1.2 Science capability	6
1.2.1 Astrophysics of stellar environment	6
1.2.2 Extragalactic science	9
1.2.3 Exoplanets	11
1.2.4 Spectroscopy with NEF	12
2.0 Engineering	14
2.1 Design concept	14
2.1.1 The NEF instrument	14
2.1.1.1 Optical design	14
2.1.1.2 Speckle chromatism	15
2.1.1.3 Scattered light	15
2.1.1.4 NEF Operation	16
2.1.2 Adaptive optics	17
2.1.2.1 The densely actuated deformable mirror M2	17
2.1.2.2 Internal wavefront sensor	17
2.1.2.3 Guiding system	18
2.1.3 The phase-mask coronagraph	18
2.1.4 Detector and data processing	20
2.1.5 Estimated performances	20
2.1.6 Additional Options	21
2.1.6.1 Achromatic Interfero-Coronagraph	22
2.1.6.2 Holographic chromatism corrector	22
2.1.6.3 Spectro-imager	22
2.1.7 Conclusion	23
2.2 Technology readiness	25
2.2.1 Phase-mask thickness	25
2.2.2 Phase-mask radius	26
2.2.3 Centering	26
2.2.4 Chromaticity	27
2.2.5 Phase-mask shape	27
2.2.6 Deformable mirror and dark-hole process	28

2.3 Development schedule and Integration & Test plan	30
3.0 Cost estimate	31
4.0 References	32

1.0 Science

1.1 Executive Summary

This study report follows the proposal (Moutou et al, 1998) of a coronagraphic camera for the Next Generation Space Telescope. Its prime goal is to attain 10^9 dynamic range in red light across a 1'' field-of-view, for the direct detection of Earth-like exo-planets orbiting nearby stars. For the time span of NGST implementation, no other space or ground-based program is expected to provide images of such faint objects in the vicinity of comparatively bright stars. NEF will thus bring new results in this area of astrophysics, probing more stars expected to show closer and smaller planets. This can prepare the detailed infra-red spectroscopy of exoplanets with forthcoming larger interferometers such as Darwin/IRSI (Léger et al. 1996) and TPF (Angel & Woolf 1997). A diversity of other astrophysical processes, related to the origins and formation of structures in the Universe, can be explored with NEF in the Galaxy and at cosmological distances.

With respect to previous instruments such as HST's Faint Object Camera (originally proposed by one of us but made inoperative for coronagraphy by the COSTAR modification of HST) the 10^9 dynamic range now targeted is expected to arise from several innovations: a phase mask, dark-speckle imaging and dark-hole optimization. The latter alone is shown by Trauger et al. (1999) to provide remarkable images of exo-planets at infra-red wavelengths. We expect similar performance with higher resolution at visible wavelengths, using the two other techniques in addition.

After a trade-off analysis regarding the achievable contrast, the performance of detectors, and the angular resolution, we have concluded in the case of NGST that 750-950 nm is the most suitable wavelength range for exoplanet imaging. The contrast in the visible and near infra-red is quite similar, but other advantages have to be considered:

- 1) A high angular resolution is achievable in the visible; it provides access to a larger sample of stars and reduces the contrast dust emission/planet in the detected system.
- 2) Visible detectors have higher efficiency in terms of readout noise and quantum efficiency.
- 3) Dark-speckle analysis can increase the image dynamic range (related to 2)

In the thermal infra-red (20_μm) the star/planet contrast improves to 10^6 , but exoplanets are definitely undistinguishable from their parent star in terms of angular resolution.

The better angular resolution at 0.8_μm (20mas) makes Earth-like planets detectable. The angular separation of an Earth-like planet from its parent star at 10pc is about $5_\lambda/D$. High-contrast imaging can be achieved with NEF for such a separation.

NEF will benefit from the large mirror size and space orbit of NGST. However, the difficulty of exoplanet detection requires the most advanced techniques of wavefront control, coronagraphy and data analysis.

The stellar light is rejected in several steps:

- Internal adaptive optics

- Phase-mask coronagraphy [Roddier & Roddier 1997]. The halo is then 10^{-6} . This coronagraph allows probing the field very close to the star, down to the diffraction limit ($0.02-1''$), which is not possible with classical Lyot coronagraphy.
 - Optimization of the adaptive optics with the « dark hole » algorithm [Malbet et al. 1995], which brings the halo to 10^{-7} in the area of interest.
- « Dark-speckle » data processing [Labeyrie 1995], which allows to gain an additional factor 100 if all the conditions are met.
- The global scheme of NEF is shown in Figure 1, for an overview of the operational suite.
- Performance simulations are presented in this report, and the instrumental feasibility is discussed (sections 2.0). Alternative options to the basic design are given in section 2.1.6

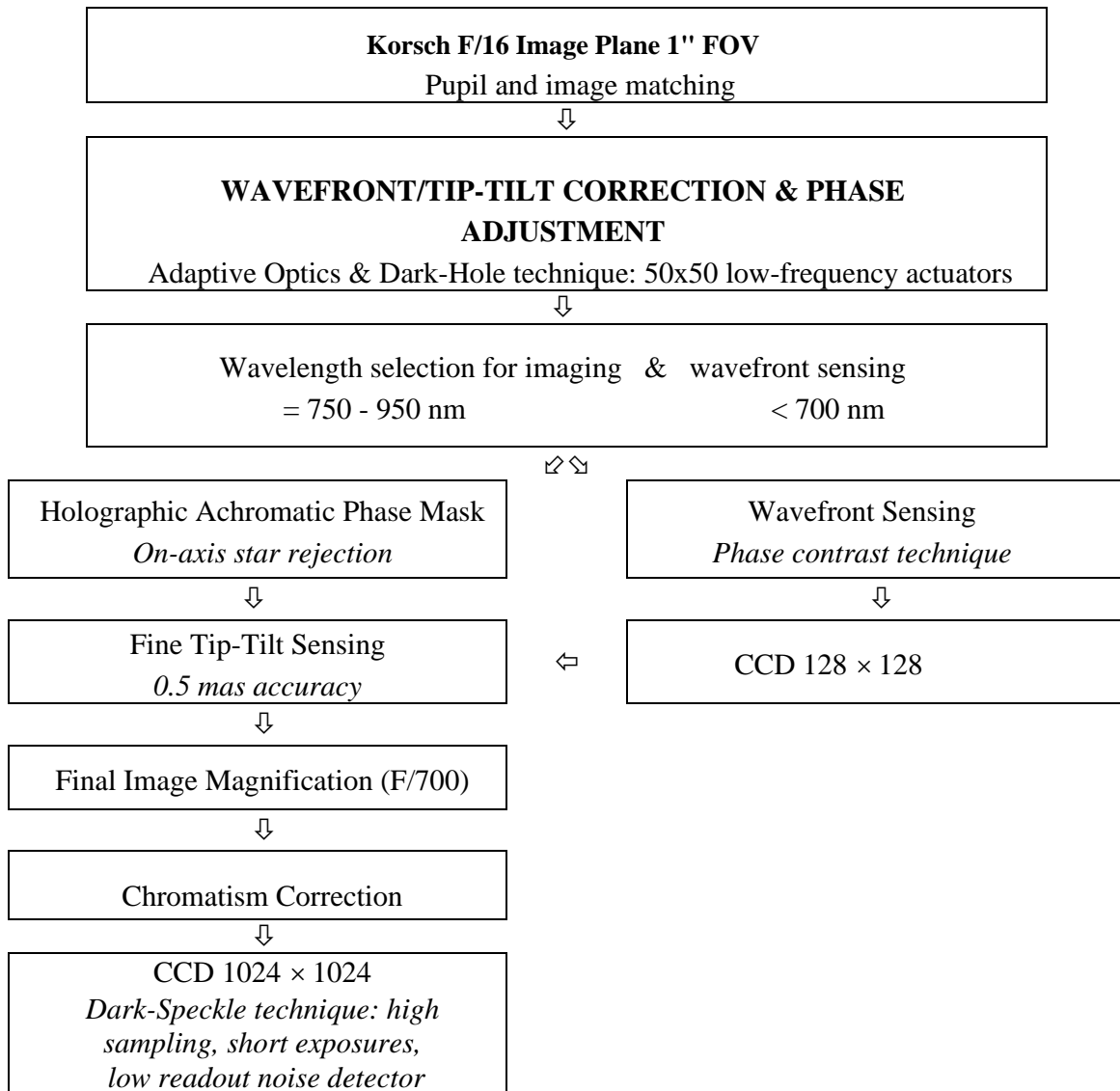


Figure 1: Functional Diagram of NEF

1.2 Science Capability

We review here some of the astrophysical issues which can be explored with NEF, taking advantage of both angular resolution and dynamical range. The diffraction halo of any point source can be imaged with a contrast up to 10^9 .

Figure 2 summarizes the actual performance of NEF and lists the achievable objects which could be detected in direct imaging. The average contrast over the field can be turned into the actual brightness ratio of the object of interest, with respect to the central, masked point source. The corresponding maximum magnitude of this point source is also given.

The numbers have been deduced from the numerical simulations, which results are described in the main core of this report, section 6. We assumed here a detector readout noise of 1 electron/pixel and an image gain of 10^6 (peak/diffracted halo contrast).

1.2.1 Astrophysics of stellar environment

Multiple systems

The high sensitivity coronagraph will observe binary systems containing a low-mass star: white or brown dwarves, which statistical distribution is poorly known at this stage. These studies could provide new data for the initial mass function of low-mass stars, the link between giant planets and stars [Burrows et al. 1997, Kulkarni 1997]. The recent discovery of the brown dwarf GL229B in a binary system [Nakajima et al. 1995] and its intensive analysis have stimulated the interest for such objects where physical processes and chemical nature are at early age.

Only a few low-mass companions are known at present time, among the brightest and most massive ones. The whole range of mass, age stellar distances and luminosity will be covered by multiple imaging detection, which would allow a more extensive study of their

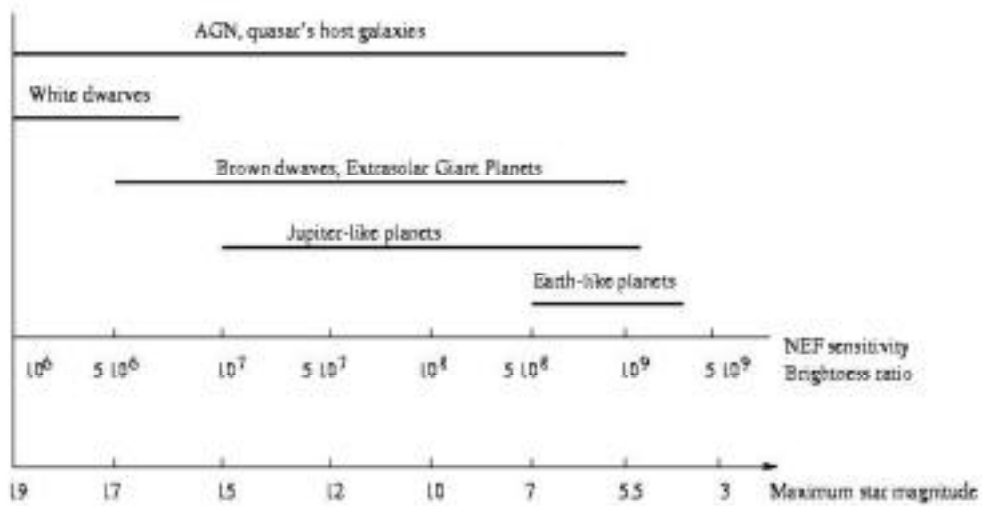


Figure 2: Diagram showing the observable objects for increasing brightness ratio - or image contrast -, within a field-of-view of 1''. Each value of brightness ratio corresponds to a maximum magnitude of the central object, given NEF sensitivity (Figure 12).

properties.

It is also worthy to investigate whether or how the birth of brown dwarfs is related to the formation of planetary systems. Telling planets and brown dwarfs apart is much more difficult. It is likely that the two classes cannot be simply divided, and that a powerful coronagraph and spectroscopy is required to differentiate between them.

We need to study a sampling of white dwarfs orbiting nearby stars to solidify our understanding of their origin and evolution. An accurate assessment of the population density of white dwarfs in the Galaxy is important for determining the Galaxy's age.

Circumstellar disks

Extended circumstellar environments such as disks and envelopes are privileged targets for NEF. They could be studied around a large sample of stars of various ages. Even thin disks surviving a strong dissipation period could be imaged. Reaching the closest vicinity of stars is of first interest for understanding the richest physical events taking place there: chemical evolution, gravitational perturbations induced by planets, sublimation limits...

For instance we could finally detect and precisely characterize the disks around Vega

and Fomalhaut at least to the level we have presently reached for Pictoris (Fig. 3). The inclination angle, thickness and extent of the disks and the inner voids and a proper characterization of the grain population can be determined in order to sharpen our dim understanding of what mechanisms drive the circumstellar environment (CS) in such stars. Precise high resolution imaging will clarify the radial and azimuthal symmetries or lack thereof, establish unambiguously the nature of the inner void and its boundaries, and possibly allow the detection of inner planets. The real bottom line here is the ability of NEF to reduce of the instrumental scattered and diffracted light by two-three orders of magnitude over the presently available best telescope/coronagraph combinations.

Finally, we will use this instrument to conduct a systematic deep search for more IR excess objects with the Vega-like luminosity fraction in order to get a robust statistical sample and, perhaps, to extend the sample to non main sequence stars such as "old" pre-main sequence and some "young" sub-giants. This would give us a good feeling of the possible temporal evolution of the disks, *i.e.* something that is controversial and essentially unknown at the present time.

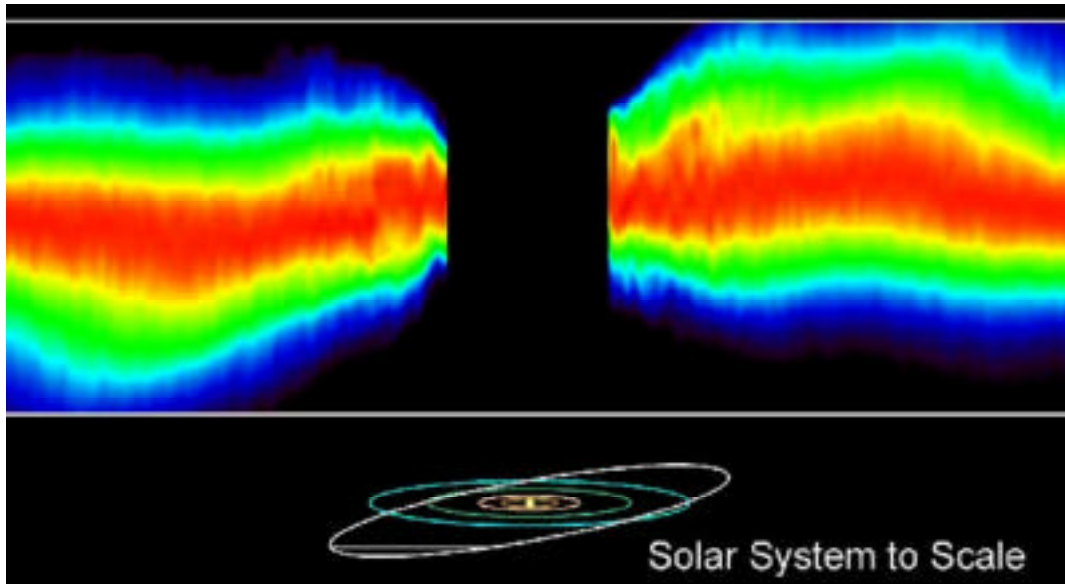


Figure 3: The warp of Beta Pictoris disk revealed here by HST, has been attributed to the presence of planets in the inner part of the disk, but this internal disk -inside the equivalent of Uranus orbit- is unobservable by present instruments, because it is over-illuminated by the star diffraction halo.

Mass losses and supernovae remnants

The study of the angular and time dependence of CS envelopes should reveal the formation of analogues of coronal holes and will tell us about cool star outflows, revealing much about the fluid dynamics of mild mass outflows. Similar observations would be worthwhile for T Tauri stars and the inner regions of planetary nebulae. The onset of complex structure in planetary nebulae occurs when the central star is still bright, probably in its asymptotic giant branch phase, making observation of close-in evolving structure extremely difficult

Mass loss is a major factor determining the evolution of stars in their later stages and a primary mystery remaining in our studies of stars before their collapse into compact objects. It may be driven by shell flashes and thermal pulses. A particularly violent phase

occurs for Mira-type variables. An application that the coronagraph makes practical is the dissection of the circumstellar nebula using the echo of the Mira pulse, as well as shells of varying optical depth (due to different observed wavelengths). Current HST observations show that the shells are ejected from novae fragment very early in their evolution. Coronagraphic observations would provide constraints on the hydrodynamic theory of the growth of swept up shells in stellar outflows, and provide us with greater insights into the evolution of these shells at very early epochs, and very close to the central source.

By 2005 the ejecta from the explosion of Supernova 1987A will strike the inner ring of its circumstellar nebula and produce intense radiation in many bands, including optical

emission lines. These will be difficult to observe against the glare of the same lines being excited by the impact, which will start as point source at the southern tip of the inner ring and expand outwards at about 0.1 " per year. A coronagraph will allow the remaining nebula to be imaged in its response to the EUV pulse, allowing a detailed time evolution study of the nebula to be made.

1.2.2 Extragalactic science

The origins of the large amounts of energy liberated by quasars, blazars and, in general, AGN (Active Galactic Nuclei), either in the form of electromagnetic radiation, jets or relativistic mass flows (cf. VLBI radio maps), still constitute today the subject of controversial debates.

In the standard model (e.g., Kormendy et al. 1996), a very massive black hole ($\sim 10^8$ solar masses) is surrounded by an accretion disk emitting part of the continuum. The broad emission lines observed in AGN spectra are thought to arise in small, very dense, hot gas clouds which are in rapid motion in the strong gravitational field of the central black hole. Photo-ionization of these gas clouds, located at typical distances of several tenths of a parsec from the central engine, has proven to be a very efficient mechanism in order to account for the observed spectra of quasars. The narrow emission lines are very likely formed in much larger clouds of rarefied gas, at several hundreds of parsec from the central engine. All these different complex regions belong to a compact nucleus, located near the center of a large galaxy (typical size over 10 Kpc) harboring the quasar (Peterson 1997). The

release of gravitational potential energy by the accreting matter onto the massive black hole certainly accounts for most of the observed nucleus activity. However, many uncertainties and questions remain on the origin and mechanism for the formation of the jets as well as on the source(s) of matter feeding the black hole.

For instance, astrophysicists wonder whether the matter being swollen by the central black hole consists of individual stars from the host galaxy or is made of gas captured during a very close interaction, or merging, with a nearby galaxy? To what extent do galactic bars facilitate the feeding of mass into the quasar, and how large a mass flow is then involved? What is the main cause of the observed quasar photometric variability? Is it due to variations in the rate of accretion? It is also not clear whether the observed evolution of the quasar luminosity function, AGN and galaxies in general, is linked to the reservoir of matter available at different cosmic times. Furthermore, did most galaxies harbor a supermassive black hole, sometimes?

We therefore easily understand that direct optical detection of the host galaxy of quasars, the jet(s), the narrow and broad emission line regions and the very surroundings of the accretion disk, ... are of the utmost importance in order to resolve the above questions. The possibility of resolving some of these structures (cf. the QSO host galaxy, NEL regions, ...) as a function of the quasar redshift and/or intrinsic luminosity ought to contribute to a much better understanding of the quasar phenomenon and of its evolution.

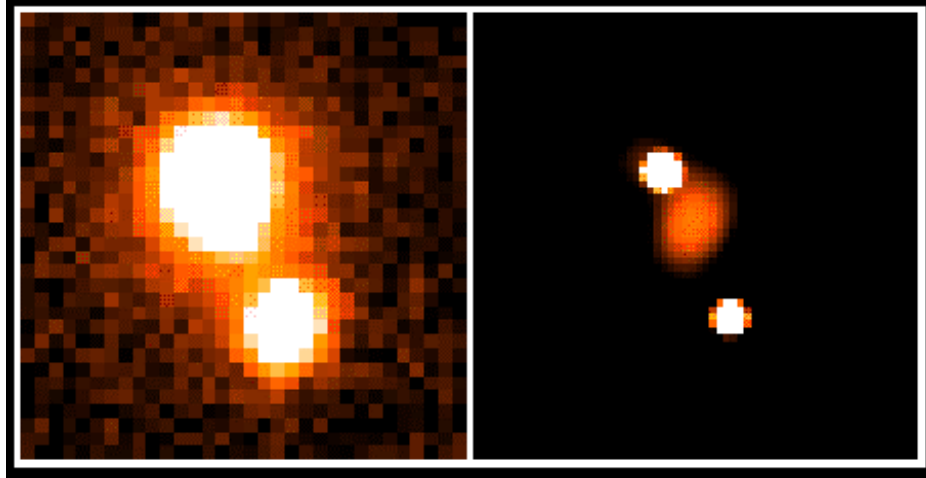


Figure 4: Images of HE1104-1805, obtained at ESO 2.2m in J band. Left: 1.4 hour exposure in a 8.8" field-of-view. Right: deconvolved image with 0.1381"/pixel [Courbin et al. 1998]. With a high-resolution, high-contrast coronagraph, detailed photometry of the lens and the galaxy host is also possible, which brings information on the lens physics

Due to the high luminosity of quasars (typically $M_V \sim -24$) and the relative faintness (from 10^3 to 10^9) and small angular extent (typically much less than 1") of the host galaxy, optical jets, narrow and broad emission-line regions and the accretion disk, it is absolutely necessary to use a coronagraphic instrument onboard a large space telescope in order to achieve direct optical imaging with a very high dynamic range at very high angular resolution.

An interesting way to further improve angular resolution when directly imaging distant AGN is to observe highly amplified quasars due to gravitational lensing. Indeed, highly amplified quasars always consist of multiple images of the background source which are significantly magnified in size. As a result, the angular sizes of the jets, flows of matter, broad and narrow emission line regions and the QSO host galaxy are enlarged, offering a large gain in angular

resolution (e.g. up to a factor 70 for the bright lensed image of the quasar HE 2149-2745) to study the extended regions of quasars and AGN. Usually, most of the extended structures are unresolved in at least one dimension, and would appear at around $B = 25$ mag or fainter. Observing these require a dynamic range of roughly 3×10^4 over an annulus extending from 0.1 to 1" in radius from the bright QSO sub-images, well within NEF capabilities.

Conversely, detailed imaging of such extended structures which are differentially magnified between the distinct quasar images can be inverted to retrieve the mass distribution of the lensing galaxy as well as the multi-wavelength shape of the source (see Wallington et al., 1996 for similar work on VLBI data and Refsdal and Surdej 1994 and Surdej and Refsdal 1994 for a general review on the observations). Finally, for those cases where the lensing galaxy is located very close to one of the multiple QSO

images (cf. UM673, BRI 0952-01, ...), the use of a coronagraph would enable to image at high angular resolution and with a very good dynamic range the structure of the deflector. Such high angular resolution observations also concern the detailed imaging of (disk?) galaxies responsible for Damped-Ly absorption lines in the spectrum of high redshift, multiply imaged quasars (cf. HE 1104-1805, Fig. 4). Detecting the red bulge population of stars associated with the putative disk galaxies would definitely solve the origin of the damped Ly absorbers.

Most surveys of the high redshift universe are strongly biased towards starburst systems. Surveys in the visible (and even near infrared) detect systems that are emitting primarily in the ultra-violet. Surveys of damped Ly systems have very different selection criteria: They are systems with high HI column densities and may well represent "typical" disk galaxies. Because of the difficulty of observing a foreground galaxy in front of a bright quasar, studies of damped Ly systems have been done in narrow lines [Steidel et al. 1994]. It will be important to make observations in broader bands to see if we can detect the red bulge population stars associated with the disks.

Finally, a special attention can be paid to faint, very close, secondary images of quasars « miraged » by lensing. A precise determination of their angular distances, brightness ratios and time delays can help to solve one of the most profound questions in astroparticle physics: is the cosmological constant non zero?

1.2.3 Exoplanets

Returning to the circumstellar environment, we now present some estimate of NEF performance in detecting exoplanets orbiting bright, nearby stars. With the discovery of the first extrasolar planets, the 23 centuries old question on the existence of 'other worlds' has turned into a scientific approach. It makes the search for 'life' outside the Solar System a plausible long term goal. A new era in astronomy has thus open, with well identified steps of a clear global strategy for the entire next century:

- a/ first images of extrasolar planets
- b/ detection of Earth-like planets
- c/ search for spectral signatures of life
- d/ multipixel imaging of extrasolar planets
- e/ multipixel spectroscopy of extrasolar planets
- f/ in situ investigation of the most interesting planet(s)

The coronagraphic NGST Extrasolar planets Finder (NEF) is not an isolated project. It is part of this strategy, by intending to make significant breakthroughs in steps a/ and b/ (first images of extrasolar planets).

Imaging exoplanets

Indirect methods for detecting exoplanets, such as radial velocity, transits or astrometry, are mostly sensitive to giant planets with short orbital periods. They are currently unsensitive to telluric planet signatures and no technics is foreseen to overgo this limit, except for interferometry. Imaging exoplanets with NEF will thus be an essential complement to previous searches: the method has a distinct bias (star distance), and it allows for instance

Contrast	Configuration	NEF sensitivity	Star distance	Number of stars
10^9	Earth at 0.8au	$mv < 5$	$d < 20$ pc	~200
10^9	Jupiter at 7.5au	$mv < 5$	$d < 20$ pc	~200
$5 \cdot 10^8$	Jupiter at 5au	$mv < 7$	$d < 100$ pc	.several 10^3
$2 \cdot 10^8$	EGP/BD at 30au	$mv < 8$	$d > 40$ pc	.several 10^3
10^8	Jupiter at 2.5au	$mv < 10$	$d < 80$ pc	.several 10^3

to detect long term period planets. Another advantage is the direct collection and analysis of planetary photons.

The brightest nearby star's surroundings will then be surveyed, for which no indirect observation has shown evidence for planetary systems up to now, with the possible exception of Proxima Centauri [Kurster et al. 1999]. Also some of the stars which show indirect evidence of orbiting exoplanets could be followed up by imaging, especially the brightest and closest ones [Mayor et al. 1999, Marcy et al. 1999].

The sensitivity gain for exo-planet detection with NEF will address the following questions:

- The proportion of stars having a planetary system
 - The number of planets per planetary system.
- A few snapshots to identify background stars from their proper motion should yield more planets than several years radial velocity or astrometric monitoring
- Determination of the orbital elements of the planets, including accurate masses in cases where radial velocity data are also available
 - Interactions with the zodiacal disk, observable as gaps.

NEF detectable configurations

The planetary system configurations (planet size, planet-star distance, distance to the observer) which can be detected depend on the

rejection factor at a given angular distance of the star.

Possible targets for different combinations of rejection factor and angular separation are given in the following table with 1-sigma level, where EGP (Extrasolar Giant Planets) and BD (Brown Dwarves) are arbitrary taken as 10 times the radius of Jupiter.

Earth-sized planets are near the sensitivity limit, but larger planets or planets slightly closer to their star could be more easily imaged, *i.e.* planets in the Habitable Zone –which size and location depend upon the star spectral type. Such a capability of detecting Earth-like planets by direct imaging is unique in the instrumentation foreseen for the next decade. Next step in the search for extra-terrestrial life will be held by the spectroscopic study of IR space interferometers such as Darwin/IRSI or TPF.

1.2.4 Spectroscopy with NEF

If a spectroscopic device is implemented on NEF (section 2.1.5.4), the following scientific issues could be also accessed:

- spectra of the highly magnified resolved structures, QSO host galaxy and lensing galaxy, from which a much more detailed modelling of the QSO structure and gravitational lens system (cf. visible and dark

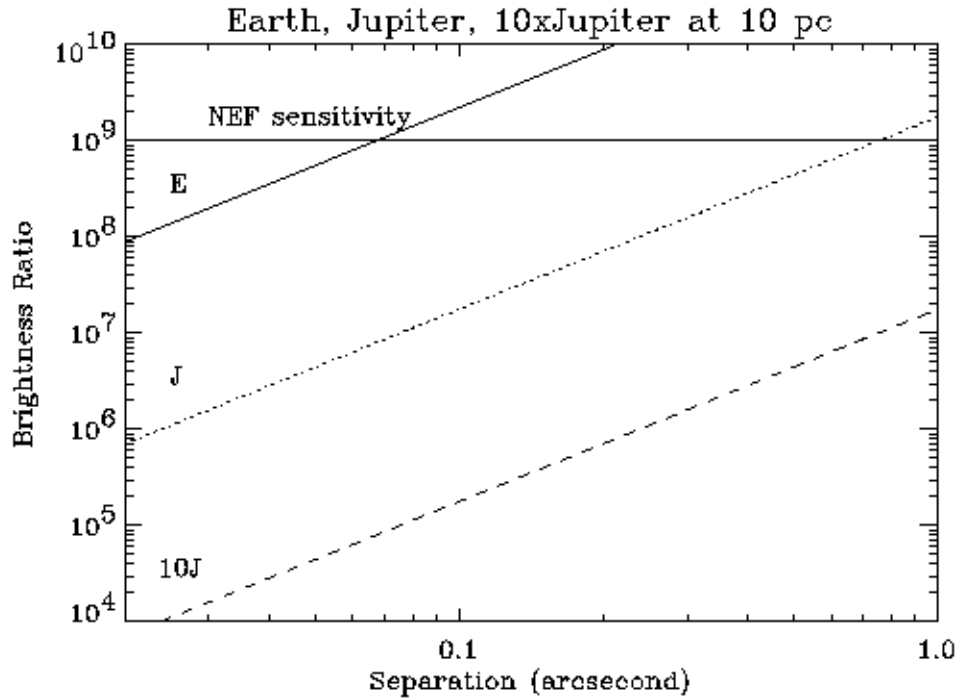


Figure 5: Brightness ratio of an exo-Earth (E), an exo-Jupiter (J) and an exoplanet with 10 Jupiter radius (10J), as a function of the angular separation, for a system located at 10 pc. NEF sensitivity presently defined as a maximum contrast of 10^9 avoids the detection of a planet of same characteristics as Earth, but planets slightly bigger in radius or closer to their star could be imaged. Giant planets all lie within NEF sensitivity limits

mass distribution of the deflector) would become feasible.

- some insights on the chemical composition of the brown dwarf/planetary atmosphere by spectro-photometry (methane, dioxygen bands). In particular we will investigate the color of the planet albedo and their time variations (in the extreme case of planets inside the habitable zone, it can even give hints for the presence of chlorophyll), with a spectral resolving power of the order of 10 to 50.

2.0 Engineering

2.1 Design concept

2.1.1 The NEF instrument

Figure 6 gives an overview of the optical design proposed for NEF. The function of most elements is detailed in the following sections. Unique features of NEF are:

- The use of an achromatized coronagraphic phase-mask (**APM**)
- The use of a Wynne lens to correct the chromatic dependence of the residual stellar speckles (**Wynne**)
- The optional wavefront analysis by phase contrast (**cpm**)
- The creation of a dark zone with minimum scattered light
- The use of short exposures with a low-readout-noise CCD (**CCD 1024x1024**) for dark-speckle analysis.

The instrument's total length is about 1250mm on this design, but it can be made more compact if needed to match the dimension of other instruments.

2.1.1.1 Optical design

As a starting point of our optical study, we have assumed NGST optics configured according to the European Korsch design with F/16 focal ratio, but NEF can accommodate different optical trains, given the very small field (1 to 5 arc-seconds) utilized.

Because coronagraphic requirements differ widely on different types of objects, the coronagraphic camera has two parallel optical trains feeding the same CCD camera or separate ones. As previously achieved in the

Faint Object Camera of the Hubble Space Telescope, the narrow optics needed allows such parallel channels with little added cost and complexity, while providing a welcome redundancy.

One channel is fully equipped for dark-speckle imaging, requiring a correction of speckle chromatism and over-sampled pixels

The second channel is much simplified, having only the essential elements of a coronagraphic camera. It also optionally has a spectro-imaging system providing up to 30 filtered images. In addition to the coronagraphy of faint objects near brighter unresolved sources, the set of filtered images is of general interest as a form of narrow-field image spectroscopy not provided by other instruments.

In the following we describe the dark-speckle channel sketched on Fig. 6.

The toroidal mirror M1 images both the pupil on the deformable mirror M2 and the focal plane on the holographic mask (**APM**). A F/200 beam is used to accommodate a 160 μ m diameter (λ F/D). phase mask. The pupil size on M2 is 10mm. The dichroic plate (**Di**) transmits the light below 750nm to the wavefront sensor (**cpm**), while the red light is reflected to the reflective phase-mask (**APM**). The phase contrast mask (**cpm**) is located on a spherical mirror to image the pupil on a 128x128 **CCD** detector with 20 μ m-pixels for a correct sampling of the wavefront.

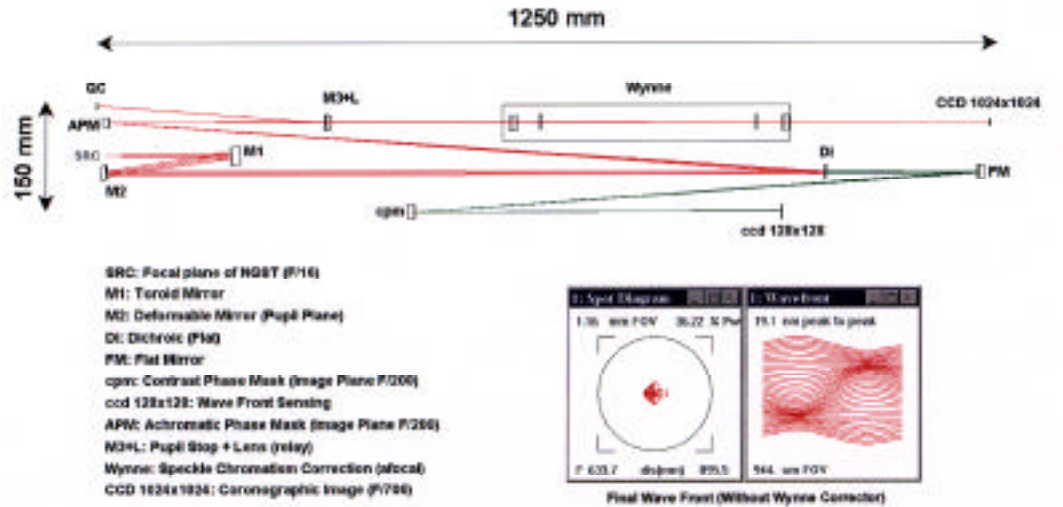


Figure 6: Basic design of the coronagraphic instrument NEF

The holographic phase mask behaves as a spherical field mirror, which provides a 1mm-pupil image on the Lyot stop (**M3+L**). Light diffracted out of the pupil by the phase-mask is re-imaged on a four-quadrant photodiode cell (**QC**) serving as the tip-tilt sensor. The photocells are slightly tilted to avoid reflecting light towards the Lyot stop. The final image has an aperture of F/700, for 25x25 pixels/speckle area sampling on the 1024x1024 CCD.

2.1.1.2 Speckle chromatism

The dark-speckle technique requires that the radial smearing of the star's speckle, due to the chromatic dependence of speckle size, be corrected. This is achieved with a Wynne corrector (represented here by 2 flat glasses), inserted between the Lyot stop and the CCD [Wynne 1979]. A holographic version of it, using a pair of reflective Bragg holograms can also be considered for a more exact correction. The result is a pupil size proportional to the inverse wavelength, providing a wavelength-

independent speckle pattern. The Wynne corrector, using a pair of afocal but chromatic lens triplets in a parallel beam, has been successfully tested on the ground-based coronagraph [Boccaletti et al. 1998]. It covers a spectral bandwidth of the order of 200nm, limited by the non-linear dispersion of available optical glasses. A holographic version, yet to be demonstrated, is mentioned as an alternate option in section 2.1.6.

2.1.1.3 Scattered light

Once diffraction from the aperture boundaries has been attenuated with coronagraphic masks, the residual scattered light in the field results dominantly from mirror bumpiness and phasing errors among the petals of a segmented NGST mirror. Malbet et al. (1995) have shown that the scattered light level can be reduced to 10^{-6} and even 10^{-7} using minor wavefront corrections with high-order adaptive optics. In the narrow fields considered here, the effect of dust particles is typically negligible with respect to mirror bumpiness

[Brown & Burrows 1990, Kuhn & Hawley, 1999].

2.1.1.4 NEF Operation

The following steps are involved in the dark-hole and dark-speckle observing mode:

- Accurate measurement of the wavefront bumpiness and guiding errors, with phase contrast and fine guidance sensors
- Application of corrections to the deformable mirror, using the dark-hole algorithm of Malbet et al., or the variant of Vakili (1999), to optimize the darkening of an annular zone surrounding the star's Airy peak
- Dark-speckle analysis of multiple short exposures: servo-noise in the actuators, kept frozen during exposures lasting about 10s, causes successive exposures to have decorrelated speckles in the stellar stray-light. Their statistical analysis, in terms of dark

speckle occurrence, provides a cleaned image where straylight can be attenuated 100 times

The dark-speckle method introduced by Labeyrie [1995] has been originally designed to detect faint companions in adaptive ground telescopes. It exploits the light cancellation caused by the random interferences in the focal plane and extracts information from the speckled halo. In the speckle pattern, the highly destructive interferences create dark regions between the speckles, called dark speckles. A planet can briefly emerge at the bottom of a dark speckle in short exposures, where the turbulence is frozen. Dark-speckle imaging has been already tested with ground-based telescopes on binary stars [Boccaletti et al. 1998] and in laboratory experiments.

The performance of coronagraphic imaging is limited by the residual speckle noise, flat-field

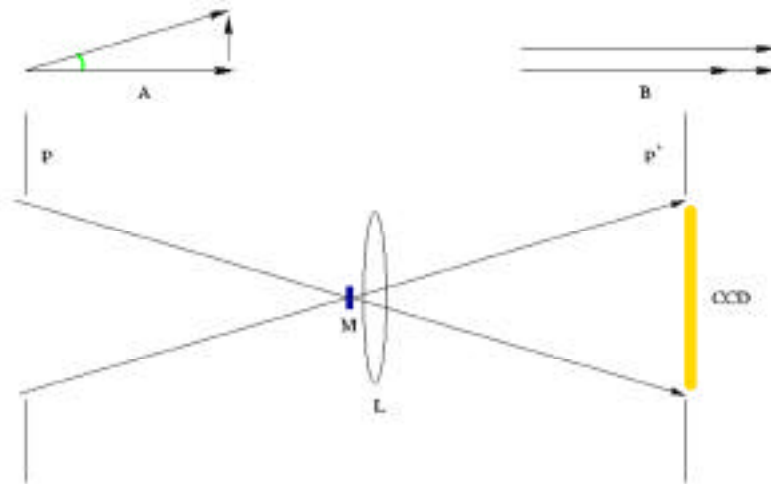


Figure 7: Principle of phase-contrast for wave analysis. *P* is the focal plane with lens *L* and relayed pupil *P'* with a CCD camera (16 bits of dynamic range and $2 e^-$ readout noise). *A*: vibration with a small phase shift represented in the Fresnel plane with its real and imaginary parts. *B*: the same vibration where the imaginary component has been made real by the mask *M*, through a 90° phase shift. The resulting vibration has an increased modulus.

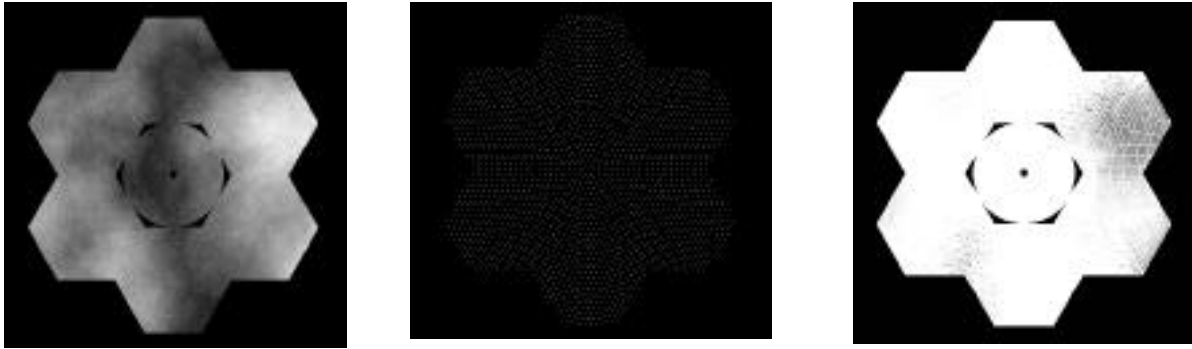


Figure 8: *Left: input phase with residual $\lambda/6$ bumpiness; Middle: Positioning of 2,500 actuators across the pupil; Right: residual phase corrected to $\lambda/68$.*

fluctuations and readout noise. Whenever possible, a calibration exposure sequence on a reference star is of interest to remove the residual non-uniform bias pattern in the image. It is expected that the residual fixed speckle pattern is rather similar for the target star and its reference owing to the stable low temperature and the accuracy of the adaptive loop.

2.1.2 Adaptive optics

2.1.2.1 The densely actuated deformable mirror M2

Adaptive optics is required to achieve the 10^9 contrast. A 1 arc-second field contains about 40×40 speckles at 0.8μ , and this corresponds to the minimal number of actuators required for controlling the wavefront at the scales involved in diffracting light within the arc-second field. For a better sampling, we consider a deformable mirror with 50×50 actuators at least. Although a wavefront corrector is considered in NASA's NGST design study, it may be inadequate for dark-speckle imaging, which requires resetting the actuators every 10s, and many of them. An internal deformable mirror is thus

inserted in the coronagraphic train. Their operating frequency, less than 1Hz, is much lower than in ground-based systems, and the stroke can be much less than $1\mu\text{m}$ if the main optics has a corresponding level of accuracy.

We have not studied the deformable mirror itself in detail, assuming that components such as described by Trauger et al. (1998) or Zhu et al. (1999) approach the desirable characteristics.

2.1.2.2 Internal wavefront sensor

The wave analysis in the present case must be very sensitive to the presence of straylight in the feet of the Airy pattern. A possible way of achieving this sensitivity involves phase contrast [Zernike 1951], using an attenuating phase quadrature mask, a few Airy radii in size, in the corrected focal plane, and a camera in the subsequent pupil image where the mirror figure is then mapped as an intensity distribution (Fig. 7). Sensitivity to mirror bumpiness at levels approaching one Angstrom has been demonstrated with phase contrast. The size of the phase-mask must be larger than the Airy peak to detect the high spatial frequencies on the mirror. Also, the contrast

can be increased with an absorbing phase-mask. A possible simplification involves the capture of the pupil pattern at the Lyot stop, where the dark background of nulled star-light lets any mirror bumps appear as brighter zones. To extract the sign of the corresponding phase errors, the 180° phase shift introduced by the Roddier phase mask has to be somewhat detuned. This form of phase contrast analyzer may thus be implemented within a spectral band outside the main science band, using a dichroic beam-splitter before the Lyot stop to feed a CCD camera.

Although not usable in ground-based adaptive telescopes, owing to the confusing shadow pattern of “seeing”, phase contrast appears of interest for wavefront sensing in space. The direct mapping of phase defects requires a modest processing power to derive the offset voltages. A 128×128 pixels CCD suffices for capturing the pupil image.

Numerical simulations have been performed for 50×50 and 100×100 actuators. A residual bumpiness of $\sim 1/68$ is expected with 2,500 actuators and $\sim 1/90$ for 10,000 actuators (Fig.8).

2.1.2.3 Guiding system

Accurate guiding is done by tip/tilting the whole deformable mirror itself. **M3** serves as a Lyot stop in the re-imaged pupil. The scattered light around the pupil is imaged by a lens on a four-quadrant photodiode. Therefore, the star centering on the mask can be re-adjusted between successive dark-speckle exposures. The precision to be achieved is of the order of 0.5 mas , which is feasible with such a device. This system receives more than 90% of the starlight and does not require a beam-splitter.

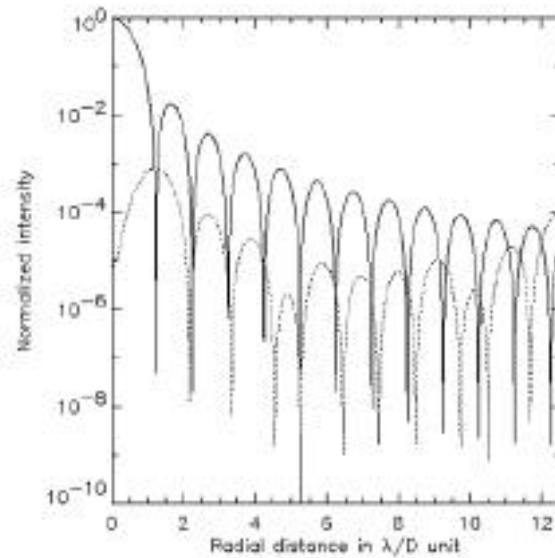


Figure 9: Logarithmic radial profiles of the PSF (solid line) and the coronagraphic image (dotted line). The diffracted light is attenuated with a factor of 50 to 100 within the range $2-10\lambda/D$

2.1.3 The phase-mask coronagraph

Classical schemes of Lyot coronagraphy use a focal mask which has to cover at least four diffraction rings for efficient removal of the outer diffraction rings from the final image. This makes it impossible to find planets closer to the star's Airy peak. We adopt the idea of Roddier and Roddier (1997), who replace the opaque mask by a transparent phase-shifting mask covering only part of the Airy peak. It provides a comparable rejection of starlight, but makes planets detectable closer to the star, down to the edge of the Airy peak. The Roddier&Roddier mask shifts the phase by 180° , rejecting most star-light outside of the pupil image formed downstream, where it is removed by the usual Lyot stop. The stop however can match exactly the geometric

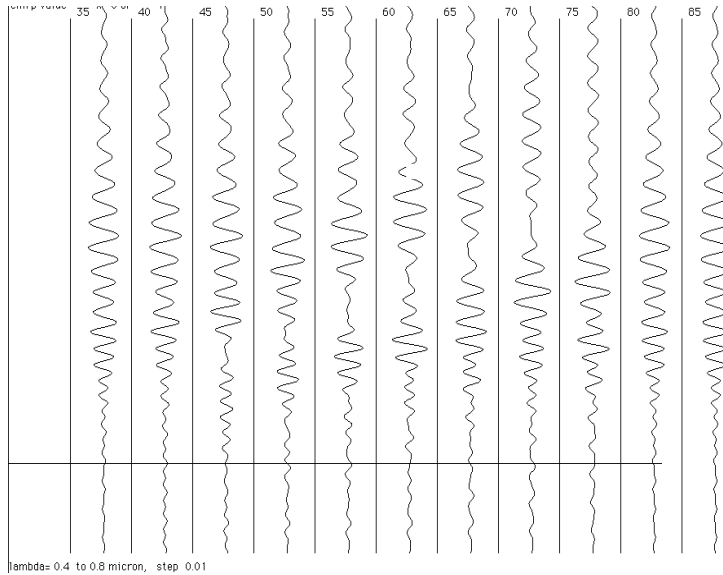


Figure 10: Radial half cross-section of a possible refractive index distribution within a reflective phase mask. The phase mask is achromated in the 400 to 750 nm range. The mask plane is horizontal, and the curves indicate vertical index profiles at increasing distances from the axis. In the bottom curves, a chirp term is added to increase the reflective efficiency.

pupil, and is therefore more tolerant of pupil obscurations (spider, etc...) than in the classical coronagraph.

Such a coronagraph can attain a rejection ratio of 100 (attenuation of the Airy wings) in the final image plane from 0.02" (λ/D) to 1". The tuning of the Roddier-Roddier mask is quite critical, and wavelength sensitive, in terms of its diameter and the optical delay. Its tuning is also sensitive to wavefront aberrations (Guyon et al.1999). Its efficiency in narrow bands has been demonstrated. The possibility to probe the field close to the Airy peak, and the tolerance to NGST's pupil segmentation makes it highly suitable for NEF. Another type of coronagraph (section 2.1.6.1), the AIC, has inherent broadband capabilities. Fig 9 shows the phase-mask radial profile compared to the instrument PSF.

However, it appears possible to make the Roddier-Roddier mask tuned across a broad spectral band if implemented in the form of a wavelength-multiplexed Bragg hologram

[Labeyrie, 1999]. A flat mirror with a bump can indeed be made in the form of a Bragg structure, in which case it can be reflective at a given wavelength, and transparent for others. Such structures, implemented in transparent materials where the refractive index is modulated, can be multiplexed for working at multiple wavelengths. Each component is then independent, in terms of its optical effect, so that the diameter and phase shift of a phase mask made in this way can be adjusted separately for each wavelength.

Tri-dimensional distributions of refractive index having such properties were calculated (Fig. 10). Such holograms can in principle be produced by holographic recording in photopolymer materials or by evaporating multiple thin-films through tiny annular masks of different sizes. Steps are taken in our group towards developing such components.

The wavelength sensitivity of the phase shift requires a relative spectral bandwidth smaller than 1:50 (20nm at 1 μ m) to keep the residual

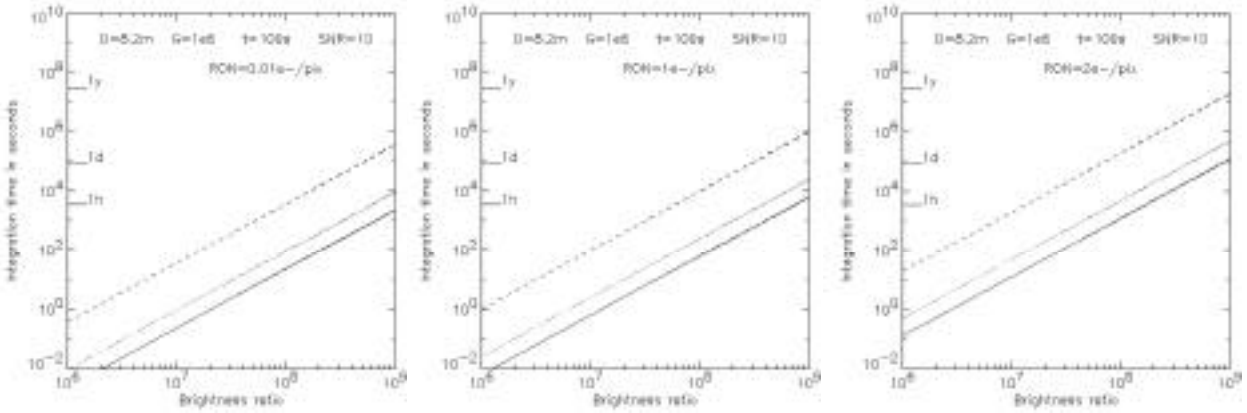


Figure 11: Expected performance of NEF, based on theoretical studies combining dark-speckle model and read-out noise. The integration time is given as a function of the brightness ratio for 2.5 (solid line), 4 (dotted line) and 8 (dashed line) magnitudes star. The calculation has been made for $0.01 e^-/\text{pix}$ (left), $1 e^-/\text{pix}$ (centre) and $2 e^-/\text{pix}$ (right) read-out noise.

intensity below 1%, in accordance with the calculations of Roddier & Roddier (1997). A holographic phase mask therefore has to incorporate 10 Bragg stratifications for covering a 200nm range. Achieving this with adequate reflective efficiency remains to be demonstrated, and we take steps towards fabricating samples.

2.1.4 Detector and data processing

With 25×25 pixels per speckle area, the sampling needed for 100x darkening through dark-speckle analysis, and 1 arc-second of field, the CCD sensor must have 1024×1024 pixels. A very low readout noise, not exceeding $2 e^-/\text{pixel}$, is necessary for efficient dark-speckle analysis. As the algorithm requires many short exposures, CCD readout with multiple outputs is desirable for fast readout with moderate pixel frequencies. State-of-the art CCDs now reach the $2 e^-/\text{pixel}$ noise level at low readout frequencies, and further improvements are expected in the coming years.

The data flow is estimated as 2 MB per exposure (from 10 to 100s). Considerable data compression is achievable on-board by applying the dark-speckle algorithm to the data cube of successive frames. The resulting cleaned image obtained after several hours of exposure is 2Mbytes, and thus transferable to Earth like ordinary images. But the option of saving the raw data cubes should be preserved, if compatible with the data system limitations.

2.1.5 Estimated performance

A global simulation, including numerous short exposures, phase-mask coronagraph, and dark-speckle analysis, is presented in figure 13. It assumes a 7-element primary mirror; a Kolmogorov spectrum for the mirror bumpiness; adaptive optics with 2500 actuators, providing a frozen pattern of wave bumpiness during the 10s exposures; an achromated phase-mask through the 200nm spectral band; uniform scattered light at 10^{-6} relative intensity (further simulations should attempt to use a more realistic radial

dependance of the scattered light). Readout noise and photon noise are included.

The numerical simulations were achieved by calculating the successive diffraction patterns with different actuator settings, providing residual bumpiness within the Rayleigh tolerance, and their propagation through the phase mask coronagraph. Weaker Airy patterns are incoherently added to the short exposures for simulating the planetary companions. After intensity scaling, both photon noise and read-out noise are introduced in each simulated 10s exposure. Dark-speckle analysis is applied to obtain the "cleaned image", and classical long exposures are also generated by co-adding the exposures, for verifying the dark-speckle gain. Figure 11 describes the sensitivity of the instrument, in terms of limiting magnitude for

a 28 hours dark-speckle observation. Read-out noise is strongly constraining. With a nearly noise-free photon-counting detector, it is possible to reach a 10^9 brightness ratio for a 6th magnitude star. In the same integration time, a CCD with $1e^-/\text{pixel}$ leads to a 5 limiting magnitude. The efficiency is dramatically decreased if the read-out noise reaches $2e^-/\text{pixel}$. Longer integration is then required to obtain a similar sensitivity.

Figure 13 shows a simulation assuming a 3rd magnitude star with 28 hours exposures. Two companions with intensity ratio 10^7 and 10^8 are visible in the vicinity of the phase mask. Better efficiency can be obtained with attenuated phase errors (to reduce the scattered light at the level of 10^{-6}), lower read-out noise ($1e^-/\text{pixel}$ instead of $5e^-/\text{pixel}$) and wider spectral range.

The computer power available for these simulations, although appreciable, did not allow generating enough exposures to reach the expected 10^{-9} level for planet detection. This should improve with faster routines.

2.1.6 Additional options

Additional optional devices can further push the exo-planet detection efficiency of NGST, but may increase the cost and complexity. First is the incorporation of the many-actuator adaptive system up-stream in the NGST train, so that the whole suite of instruments can benefit from the better image quality.

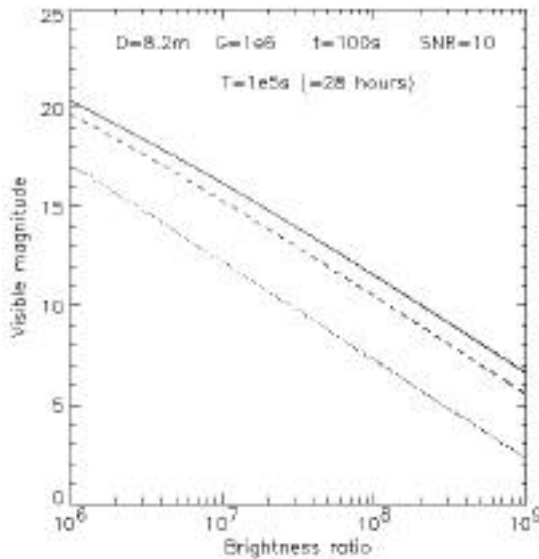


Figure 12: Sensitivity in magnitude as a function of the brightness ratio, for $0.01e^-/\text{pix}$ (solid line), $1e^-/\text{pix}$ and (dashed line) $2e^-/\text{pix}$ (dotted line) read-out noise. The total integration time is about 28hours.

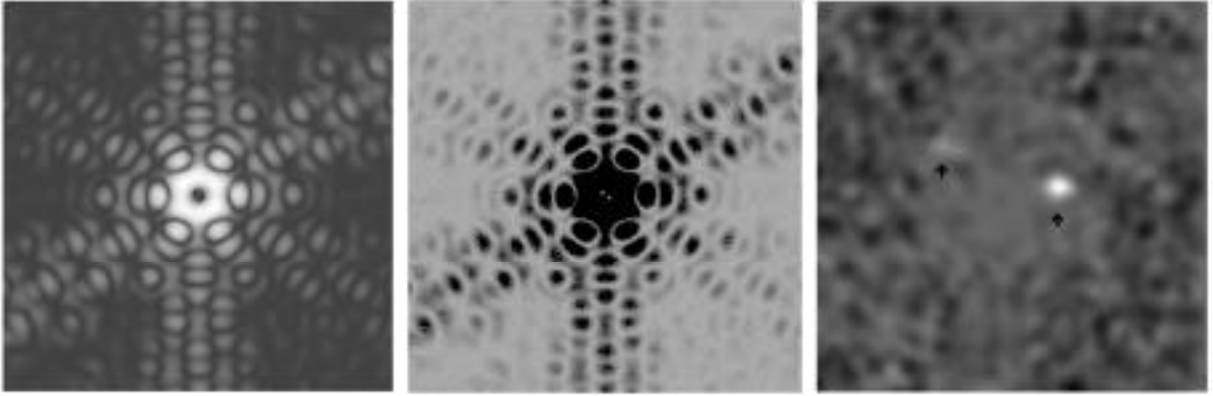


Figure 13: Coronagraphic observation of a 3^{rd} magnitude star with 2 companions of brightness ratio $R_1=10^7$ and $R_2=10^8$, and with angular separation of $\rho_1=70\text{mas}$ and $\rho_2=100\text{mas}$. The residual phase defects are corrected with 2500 actuators adaptive system and re-shaped each 10s to enable dark-speckle analysis. A read-out noise of $5e^-/\text{pixel}$ is added to each frame. We have considered a simple phase-mask with a bandwidth of only 10nm. We present the coronagraphic long exposure (left), the dark-speckle clean map (middle), and finally, a χ^2 test obtained on the dark-map subtraction, revealing the presence of the 2 companions (right, arrows). The level of scattered light is about 10^{-5} (relative to the unmasked Airy peak) but can be improved with at least a factor of 10. In such condition, the brightness ratio theoretical limit is about 10^7 , which is consistent with the present simulation.

2.1.6.1 Achromatic Interfero-coronagraph (AIC)

The alternate coronagraphic concept demonstrated by Gay & Rabbia (1996) (Rabbia et al. 1998) brings an ingenious solution to the chromatism problem. However it raises other difficulties, regarding the adjustment of the wave amplitudes for deep nulling, the loss of half the planet's light, and the symetrization of the image. Like the phase-mask coronagraph, it can find companions edging inside the Airy peak.

2.1.6.2 Holographic chromatism corrector

Two holographic mirrors can replace the Wynne lenses for the correction of speckle chromatism, if their curvature depends on the wavelength. The first mirror has a concave

shape while the second is convex. This can provide a more exact solution than the lens system, and also avoids potential problems with cemented triplet lenses in space. The reflective efficiency reachable has to be assessed on prototype elements, the fabrication of which is now considered.

2.1.6.3 Spectro-imager

A Courtès-type spectro-imager can be inserted in the simplified coronagraphic channel to produce some 30 filtered images of the 1-4 arc-second field. This adds powerful capabilities to the instrument, not only for obtaining spectral information on exo-planets first detected with the dark-speckle channel, but also on remote galaxies or other small and faint objects. Further work is under way to explore the

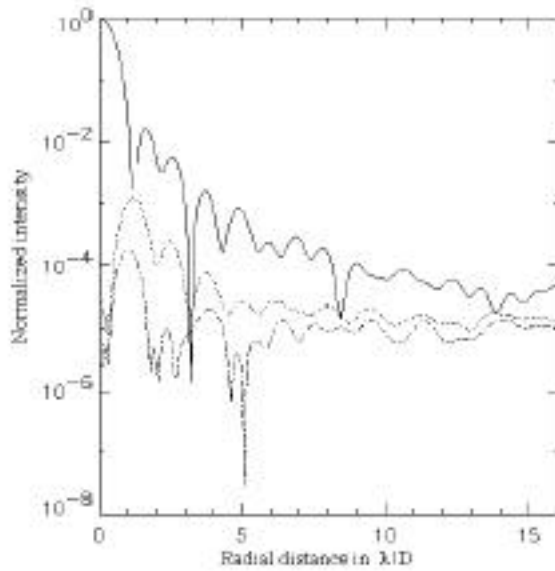


Figure 14: Radial averaged profile of the PSF (solid line), the coronagraphic image (dotted line) and the scattered light (dash-dotted line), for the simulation of Fig.13. The simulated phase defects correspond to an averaged scattered light of 10^{-5} (relative to the Airy peak). Given the sampling of 10×10 pixels/speckle area, the maximum achievable brightness ratio using dark-speckle is about 10^7 .

photosynthetic absorption bands in heavily vegetated planets.

Some critical elements of NEF, requiring more development, are the dense adaptive optics, the achromatic phase-mask coronagraphy low-noise detectors.

To allow the detection of low-separation objects such as Earth-like planets, NEF is designed for visible imaging, but the concept can be extended to the near IR, where the resolution is decreased, and the probability of detecting photosynthetic absorption is perhaps lower.

optimal integration of both imaging channels and the spectro-imager.

2.1.7 Conclusion

The two following tables summarize the instrument requirements and performances of NEF. We have demonstrated the feasibility of ultra-high contrast imaging in the visible with NGST, allowing the direct detection of Earth-like extra-solar planets. Planets in the 'Habitable Zone' are indeed detectable and the spectro-imaging option may show

Requirements :

Wavelength range	7500 - 9500 Å
Pixel sampling (Binning without adding noise)	<25x25 pixels/speckle area for 10^{-6} scattered light level <10x10 pixels/speckle area for a 10^{-7} scattered light level
Pixel size	20µm
CCD size	1024x1024
Number of actuators	50x50
Frequency of active control	10mHz ~ 1Hz
Exposure time	0.1s ~ 100s
Guiding precision	0.5 mas
Phase mask size	160µm
Final focal ratio	F/700
Read-out noise	1/2e ⁻ /pixel

Performances :

Field of view	1"
Spatial sampling	< 25x25 pixels/speckle
Spatial resolution	diffraction limited at 0.85µm
Spectral resolution	Low (<5)
Observing modes	ultra-high contrast imaging
Optics throughputs	TBD
Scattered light	not applicable
Illumination uniformity	TBD
Accuracy of sky subtraction	not applicable
Spatial & spectral accuracy	super resolution (few mas)

2.2 Technology Readiness

Achromatic phase-mask is one of the most critical component of NEF. Some numerical simulations have been carried out to assess the level of feasibility. In the following we give the simulations results concerning the requirements on thickness, radius, spectral bandwidth and centering of the phase-mask.

2.2.1 Phase-mask thickness

With a phase-mask made in TiO_2 , the theoretical thickness is 312.5nm. Current technology allows thickness uncertainty down to 1nm. We investigate the effect of a uniform thickness variation compared to the theoretical value. Results are summarised in Fig. 16. It shows the residual intensity relative to the theoretical case as a function of the defect

amplitude. In addition, radial profiles of the coronagraphic images are presented. It comes out that residual intensity less than 1% can be achieved if the global thickness is controlled down to 3nm. The residual intensity exhibits a square-law dependence with thickness variation.

We also evaluate the effect of a non-uniform thickness fluctuation on the mask surface although such a defect is highly unlikely. With a typical defect size of 1/10 of the mask diameter and 1nm-rms amplitude, the residual intensity is about 1%. More critical are the low frequency thickness variations (see section phase-mask shape).

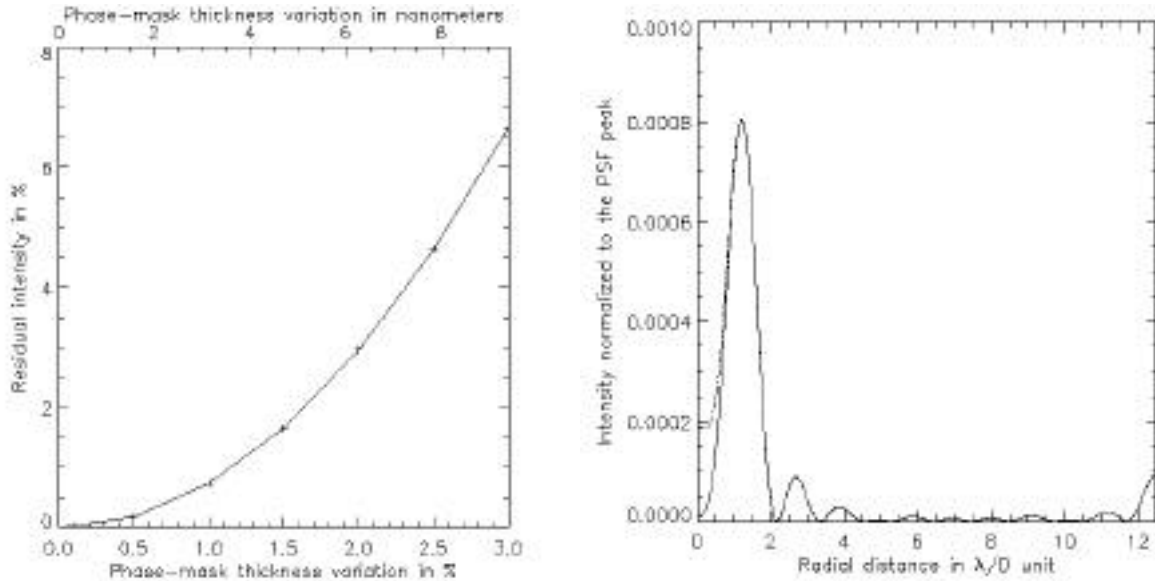


Figure 16: Left: Residual intensity in the coronagraphic plane as a function of the **thickness variation** expressed both in % and in nanometers. Right: Linear radial profiles of coronagraphic images obtained with an optimised phase-mask (solid line) and with a 1% variation of the mask thickness (dash-dotted line). Most of the residual energy is concentrated in the centre while the effect is almost negligible on the attenuated rings ($<1\%$) where exoplanets are expected to be found.

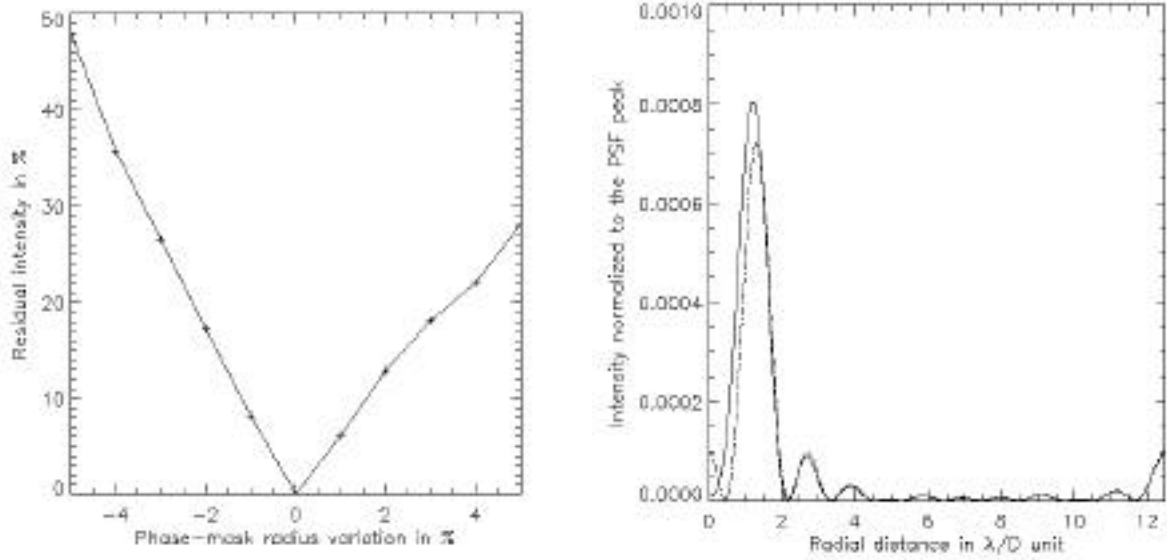


Figure 17: Left: Residual intensity in the coronagraphic plane as a function of the **phase-mask radius variation** expressed in %. The area between 0 and 2 λ/D is not taken into account to assess the residual intensity. Right: Linear radial profiles of coronagraphic images obtained with an optimised phase-mask (solid line) and with a 1% variation of the mask radius (dash-dotted line).

2.2.2 Phase-mask radius

We now investigate the effect of changing the mask radius on the resulting image. The theoretical radius is $0.53 \lambda/D$. We consider fluctuations of the order of $\pm 5\%$ of this radius. Results are displayed in Fig. 17. It shows that small variations of 1% of the mask radius induce a residual intensity of about 10% which is not tolerable. However, the mask diameter can be adjusted to match the precision allowed by the current technology. For a coronagraphic plane imaged at $F/D=200$, the optimal mask diameter is about $200\mu\text{m}$. Therefore 1% variation represents $2\mu\text{m}$ uncertainty. Since the behaviour of residual intensity is linear, a precision of $0.1\mu\text{m}$ is required to achieve 1% residual intensity in the coronagraphic plane.

Such a goal is achievable with current technology.

2.2.3 Centering

In order to assess the required centring tolerance, the star was tilted with respect to the mask. We found a residual energy of 5% for an off-axis of 0.5mas . But most of the residual energy is concentrated around the mask, and the centring defects have very small effects on the PSF wings. In addition to fine guidance sensor foreseen on the NGST, an internal tip/tilt correction is required to achieve a centring accuracy of 0.5mas . Residual intensity presented in Fig. 18 exhibits a square-law dependence. With the light rejected by the Lyot stop, a bright, unmasked image of the star can be formed to monitor precisely the centring with a 4-quadrant diode.

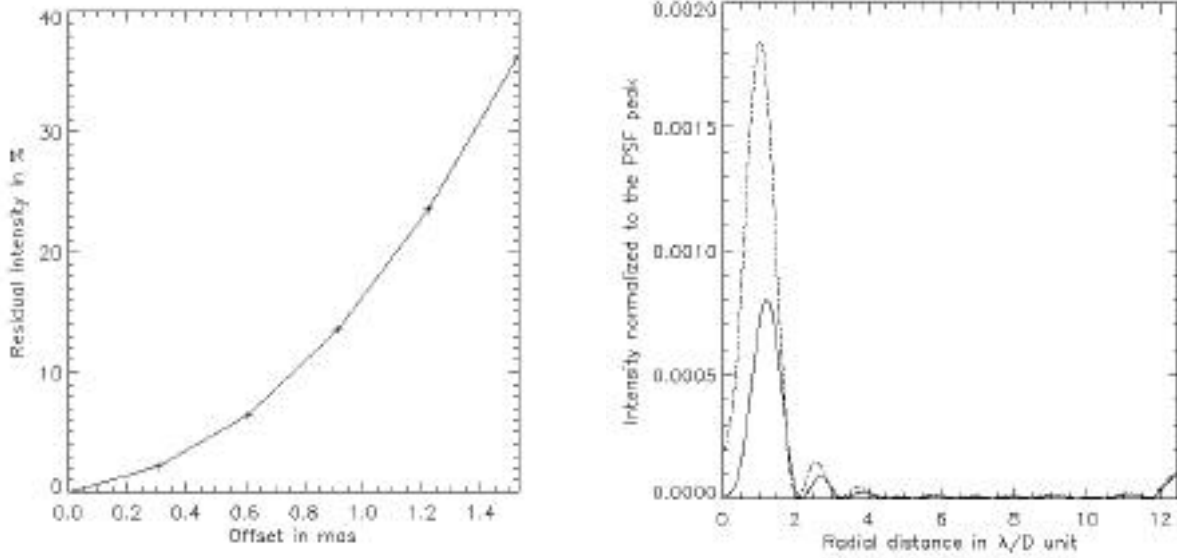


Figure 18: Left: Residual intensity in the coronagraphic plane as a function of the **offset variation** expressed in mas. Right: Linear radial profiles of coronagraphic images obtained with an optimised phase-mask (solid line) and with an offset of 0.6mas (dash-dotted line).

2.2.4 Chromaticity

The phase-mask radius and thickness are both directly related to the wavelength. Here, we investigate how critical the instrument chromaticity is and what spectral resolution can be used. The Airy pattern is simulated by adding 10 monochromatic beams centred on $1\mu\text{m}$, with a resolving power of 20 to 100.

Results are presented in Fig. 19 The instrument requires a spectral resolution larger than 50 to keep its efficiency (residual intensity 1%). It is of the same order of the theoretical prediction ([Roddier&Roddier 1997]). To collect more flux and conserve the achromaticity over a spectral band pass of 200nm, we consider the study of a holographic phase mask.

2.2.5 Phase-mask shape

It is suspected that the fabrication process could provide a non-uniform thickness with a

typical gaussian shape. This effect is the most critical in this study. We investigate various phase-mask shapes with straight gaussian edges and concave or convex profiles. Then, we compare the coronagraphic intensity obtained respectively, with a perfect mask (straight edges), and a gaussian mask.

Since the convex shape features has straighter edges, it appears the more convenient solution. Once the process of fabrication will be identified, some solutions should be found to decrease the residual intensity in the coronagraphic plane down to 1%. However, it seems possible to reduce this gaussian shape defect by adjusting the radius of the mask.

The phase-mask efficiency has been found sufficiently stable over the defects studied in these simulations and allowed by the current

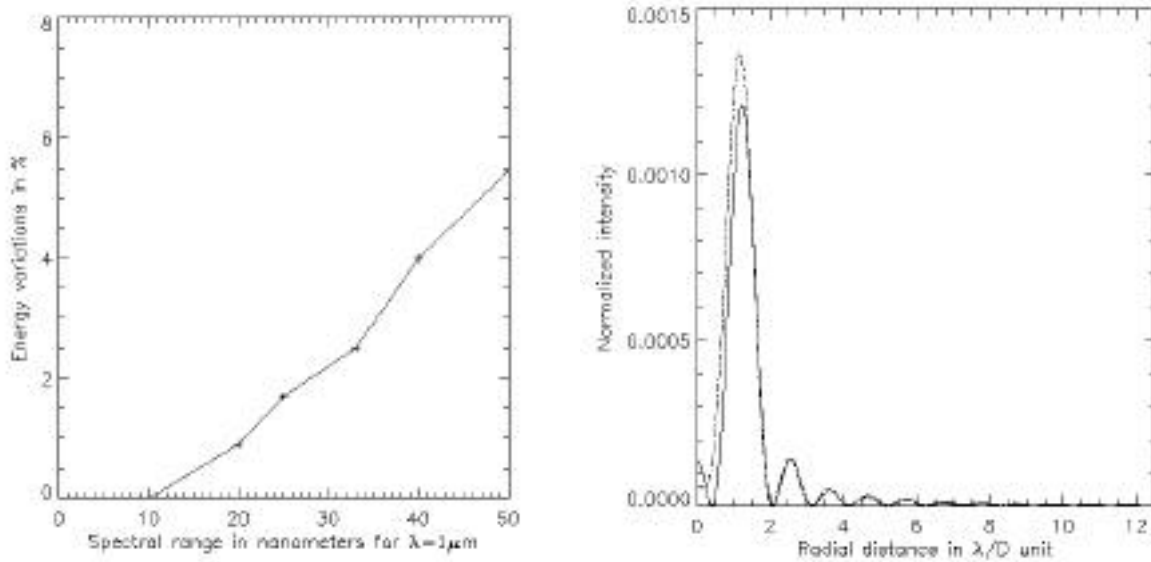


Figure 19: Left: Residual intensity in the coronagraphic plane as a function of the *spectral range* (in nanometers). Right: Linear radial profiles of coronagraphic images obtained with an optimised phase-mask in monochromatic light (solid line) and with a spectral range of 20nm in polychromatic light (dash-dotted line) equivalent to a resolving power of 50 at $1\mu\text{m}$.

technology. Nevertheless, the defects affecting the mask centring and the phase-mask shape must be paid more attention in the design and during operations, as a slight shift to the optimal values may have a critical effect on the residual scattered intensity.

2.2.6 Deformable mirror and dark-hole process

The deformable mirror is the second critical component of NEF. Numerical simulation have been carried out to assess the feasibility of the dark-hole technique using high-order adaptive mirror (Fig. 20). With a large number of actuators we found that such a technique enable dynamic range imaging down to 10^{-6} or even 10^{-7} relative to the Airy peak

Several types of actuators can be considered and compared for the implementation of

thousands of actuators on small surfaces (a few mm): piezo elements, electrostatic actuators, liquid crystals. Adaptive optics systems for ground-based telescope with 940 elements are already available on large area of a few tens of centimeters (USAF Phillips Laboratory).

Some micro technologies are currently under development to realize high-density adaptive optics with inter-actuator spacing of less than 1mm. Ealey and Wheeler (1990) have reported a study on integrated wavefront corrector with 100 elements on 1cm^2 using piezoelectric PLZT actuators and similar devices with thousand elements are foreseen.

Another promising technique using membrane mirror has been studied for the SUBARU telescope (Takami & Iye 1994). The membrane is used as a reflective surface and as an electrode. They are less expensive than

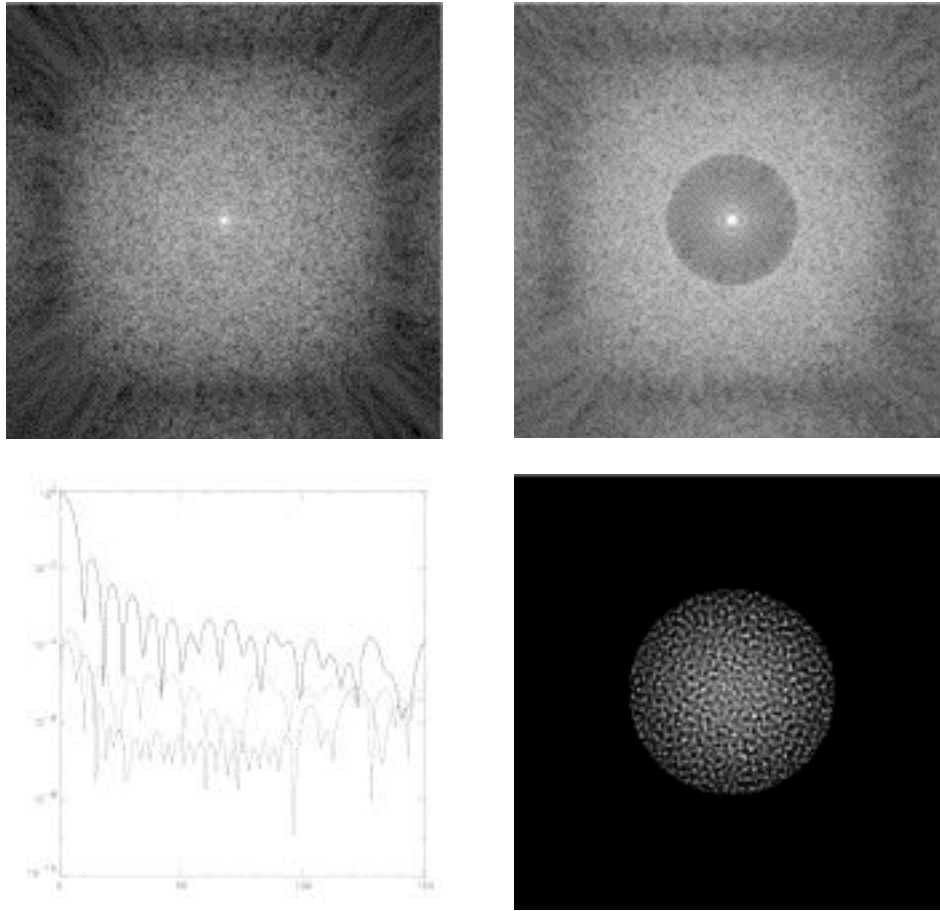


Figure 20: Results from the "Dark-Field" technique developed by the NEF study-team. Top left: NGST simulated diffraction pattern assuming $\lambda/4$ RMS phase errors (spatial scale on the 8m primary mirror is 8cm), Top right: solution dark-field after 50 iterations, Left bottom: radial intensity profiles after subtraction of a reference star: the Airy-Peak to darkened-field intensity ratio is 2×10^7 , Right bottom: piston map to apply on the deformable mirror to obtain the above solution dark-zone.

other wavefront corrector and feature a high quality surface with no hysteresis. The surface of a high-order membrane corrector with $100\mu\text{m}$ elements is not really smooth and must be coupled with a low-order corrector.

Other technique uses membrane mirrors called MEM (Clark et al. 1996). MEM are build as microchips on which thousands of actuators can be implemented, on surface as small as

1cm. The mirror elements are in fact very small and sparse, a lens array is however required to reach a fill factor of 100%.

Liquid crystals are in principal unlimited in spatial resolution with sizes as small as $10\mu\text{m}$ per elements (Bonaccini et al. 1991, Esposito et al. 1993). Their refractive index can be changed if used with polarized light and they

are more efficient in near-IR. In space, the slow response time of liquid crystals is not a limitation, but other problems arise such as the low temperature effect.

A promising design for NGST is under fabrication by Xinetics [Trauger et al. 1998]. It consists in small arrays of 21x21mm, each actuator being a 1mm element in electrostrictive ceramic. The prototype has been tested successfully and features stability of 0.2nm rms. Larger arrays can be build with several buttable modules of 21x21 elements. A qualification test of a 63x63 array is ongoing at Xinetics and JPL.

2.3 Development schedule and Integration & Test plan

TBD

3.0 Cost estimate

TBD

4.0 References

1. Angel J. R. P. & Woolf N., 1997 *Astrophysical Journal* 475, 373
2. Boccaletti A., Moutou C., Labeyrie A., Kohler D., Vakili F., 1998, *Astron. & Astrophys. Sup. Series* 133, 395
3. Bonaccini et al., 1991, *Proc. SPIE* 1543, 133
4. Brown R. and Burrows C. 1990, *Icarus* 87, 484
5. Burrows A. Marley M., Hubbard W.B. et al., 1997, *ApJ* 491, 856.
6. Clark R., Karpinsky J., Borek G., Johnson E., Clark N., 1996, *Proc. Top. Mtg. On Adaptive Optics, ESO Conf. And Workshop Proc.* 54, 433
7. Courbin F., Lidman C. & Magnain P., 1998, *A&A* 330, 57
8. Ealey M.A. and Wheeler C.E., 1990, *Integrated wavefront corrector, Proc. SPIE* 1271, 254-264
9. Esposito et al., 1993, *ESO Conference and Workshop Proc.* 48, 289
10. Gay, J. and Rabbia, Y., 1996, *CR. Acad. Sci. Paris, t.322, Serie IIb*, 265-271.
11. Guyon O., Roddier C., Graves J.E., Roddier F., Cuevas S. & Espejo C. 1999, to appear in *Applied Optics*
12. Kormendy, J. et al. 1996, *Ap. J.*, 459, L57.
13. Kuhn J. and Hawley S. 1999, *Publ. Soc. of Pacific* 111, 601
14. Kulkarni S., 1997, *Science* 276, 1350.
15. Kurster M., Hatzes A.P., Cochran W.D., Doebereiner S., Dennerl K., Endl M. 1999, *Astron & Astrophys.* 344, 5
16. Labeyrie A. 1995, *Astron. & Ap.*, 298, 544-546.
17. Labeyrie A. 1999, "Planets Outside the Solar System" *NATO Science Series C532*, Alloin & Mariotti Eds., v532, 261
18. Léger A., Mariotti J.M., Mennesson B., Ollivier M., Puget J.L., Rouan D. & Schneider J., 1996 *Icarus* 123, 249-255
19. Lyot, B. 1939, *MNRAS*, 88, 580.
20. Malbet, F., Yu, J. W., Shao, M., 1995, *Publ. Soc. of Pacific* 107, 386.
21. Marcy G.W, Butler R.P., Vogt S.S., Fischer D., Liu M.C. 1999 *Ap. J.* 520, 239
22. Moutou, C., Boccaletti, A. & Labeyrie, A., 1998, in the *Next Generation Space Telescope: science drivers and technological challenges*, C.R. du 34^{ème} Colloque international Astrophysique de Liège, 15-18 juin, p. 121
23. Delfosse X., Forveille T., Beuzit J.L., Udry S., Mayor M., Perrier C. 1999 *Astron. & Astrophys.* 344, 897
24. Nakajima T., Oppenheimer B.R., Kulkarni S.R., Golimowski D.A., Matthews K., Durrance S.T. 1995, *Nature* 378, 463

25. Peterson, B.M.: 1997, Book "An Introduction to Active Galactic Nuclei", Cambridge University Press
26. Rabbia Y., Baudoz P., Gay J., 1998, "NGST Science Drivers and Technological Challenges" Proceedings 34th Liege International Astrophysics Colloquium, p. 279
27. Refsdal, S., Surdej, J.: 1994, Reports on Progress in Phys. 56, 117
28. Roddier, F. and Roddier C. 1997, Publ. Soc. of Pacific 109, 815
29. Steidel C.C., Pettini M., Dickinson M., Persson S.E. 1994 Astron. J. 108, 2046
30. Takami H. & Iye M., 1994, Adaptive optics in Astronomy, Proc. SPIE 2201, 762
31. Trauger J et al. 1998 proposal in response to NASA NRA 98-GSFC-1
32. Wallington, S., Kochanek, C.S., Narayan, R.: 1996, AJ. 465, 64
33. Wynne C.G., 1979, Opt. Comm. 28, 21
34. Zernike 1951
35. Zhu L., Sun P.-C., Bartsch D.-U., Freeman W.R., and Fainman Y1999, Applied Optics 38, 168